Synthesis and characterization of non-stoichiometric cobalt nanoferrites for multifunctional applications

Ebtesam E. Ateia[1,2], Abdulalah AL-Hamzi[3,*] (iD), and B. Hussein[1]

[1] *Physics Department, Faculty of Science, Cairo University, Giza, Egypt*
[2] *Academy of Scientific Research and Technology (ASRT), Cairo, Egypt*
[3] *Physics Department, Faculty of Education et al-Mahweet, Sana'a University, Al-Mahweet, Yemen*

ABSTRACT

We report on the recognition of crystallite size, morphology, and chemical composition-controlled cobalt ferrite nanoparticles (NPs) with adaptable physical properties for multifunctional applications. The stoichiometric and non-stoichiometric cobalt ferrites ($CoFe_2O_4$ & $Co_{1.5}Fe_{1.5}O_4$) show unique characteristics due to their different redox states and excellent magnetization. The samples have been synthesized using the citrate autocombustion technique. X-ray photoelectron spectroscopy (XPS) is utilized to study the oxidation state of each element and the chemical stoichiometry composition in the samples. The magnetic loop plots show the ferrimagnetic behavior of $CoFe_2O_4$ and $Co_{1.5}Fe_{1.5}O_4$ NPs that are saturated with large values of magnetization depending on the stoichiometric/non-stoichiometric ratio. The spin states of Co^{2+} ($3d^7$), and Co^{3+} ($3d^6$) ions in the B sites have been proposed to be in both high spin and low spin states, respectively. On the other hand, Co^{2+} ($3d^7$) in the A site is usually found in high spin states. Additionally, Fe^{2+} ($3d^6$), Fe^{3+} ($3d^5$) in B sites, and Fe^{3+} ($3d^5$) in A sites are frequently found in high spin states. The shape of M–H loops for the investigated samples enables their candidature for applications in memory devices and magnetic sensors.

1 Introduction

The spinel ferrite nanoparticles NPs have an extensive range of applications in a diversity of fields due to their good physical properties [1]. They have a high potential to work as magnetic materials, even under high frequencies. They can be used in electronics and microwave appliances due to their high resistivity [2].

The spinel ferrite has a structure that can accommodate a variety of cations, some of which may have numerous oxidation states and be distributed in diverse ways at the tetrahedral (A), and octahedral [B] sites [3]. The properties of the ferrite materials depend on the replacement of different cations on both sites [4]. On the basis of cation distribution, the spinel ferrites can be divided into three types: (a) normal spinel ferrites; (b) inverse spinel ferrites;

Address correspondence to E-mail: abdalellah7389@gmail.com

and (c) random spinel ferrites [5]. The coupling of unpaired spins of metal ions is the main issue in understanding the magnetism of ferrite NPs.

If the two metal ions are shared through oxygen ions, then it can facilitate the coupling of spins via exchange interaction. Generally, ferrites exhibit ferrimagnetism due to the strong A–A ferromagnetic and A–B antiferromagnetic coupling [6].

In the spinel structure, the oxygen atom is not always located at the FCC sublattice. Their detailed positions are deformed as given by the u parameter, which reflects adjustment of the structure to accommodate differences in the radius ratio of the cation in A and B sites.

Generally, the A site is smaller in size than the B sites. A site is unable to accommodate available cations without local distortion of the sites. Thus, each A site expands by an equal displacement of the four surrounding oxygen ions, towards and along the body diagonal of the cube, to form a tetrahedral with an A − ion having cubic symmetry. However, six oxygen ions surrounding a B site are shifted in such a way that this oxygen octahedral shifts by the same amount, as the first expands. A quantitative measure of this displacement is the oxygen positional parameter u, given by the distance between an oxygen ion and the face of a cube [7].

Cobalt is a hard magnetic material that has attracted the attention of the technical community due to its unique enhanced magnetic properties, which include high saturation magnetization, radio frequency hyperthermia, high-density audio and video recording media, and medical diagnostics [8].

Transition metals (TM) occur in numerous oxidation states, which generally have various magnetic moments depending on their spin states. The spin state (low–high) depends significantly on crystallographic configurations, like (A) and [B] sites. Franco Junior et al. [9] ratified that Co ions of both 2 and 3 oxidation states can coexist, as can Fe ions in the Fe_3O_4 ferrites. Additionally, Co^{3+} in the B site favors a low spin state (LSS) although it gives rise to surprising magnetic properties. This recommends synthesizing samples with structures such as $CoFe_2O_4$, as well as $Co_{1.5}Fe_{1.5}O_4$ that are formed of TM with the desired magnetic properties [10].

In the present work, the $CoFe_2O_4$ and $Co_{1.5}Fe_{1.5}O_4$ NPs were prepared by the citrate autocombustion method. The citrate autocombustion technique, among all available synthesis methods, is intensively utilized for the preparation of homogeneous nanopowders due to its advantages, i.e., high purity, crystallinity, great control of stoichiometry, low cost, high yield, and effectiveness [11]. An attempt is made to study the effects of the substitution of the excess cobalt ions at the expense of iron ions on the characteristics and magnetic properties of the investigated samples. At the same time, the non-stoichiometric of the investigated samples are discussed. As far as the authors are aware, there is no published analysis of the factors affecting the magnetic properties of $Co_{1.5}Fe_{1.5}O_4$ nanomaterial. Indeed, at present, general research into $Co_{1.5}Fe_{1.5}O_4$ is still in its infancy. Therefore, the obtained data from this research offer a new opportunity for optimizing and improving the performance of non-stoichiometric cobalt nanoparticles where the physical properties are decisive.

2 Experimental work

The nanoparticles of stoichiometric $CoFe_2O_4$ and non-stoichiometric $Co_{1.5}Fe_{1.5}O_4$ samples were synthesized via the citrate autocombustion technique using analytical grade cobalt nitrate, iron nitrate, and citric acid ($C_6H_8O_7$). More details were discussed in the previous work [12, 13]. An X-ray diffractometer was used to scrutinize the structure and size of the crystallites (XRD). Scherrer's relationship was used to calculate the average crystallite size, and several characterization techniques were performed to study the physical properties of the prepared samples.

3 Results and discussion

3.1 Structural analyses

3.1.1 X-ray Diffraction Analysis

The structures of the non-stoichiometric $Co_{1.5}Fe_{1.5}O_4$ and stoichiometric $CoFe_2O_4$ nanoparticles are examined using an X-ray diffraction (XRD) technique. The XRD pattern is shown in Fig. 1, compared and indexed with ICDD card no. (01-083-3117) [14]. The formation of a single-phase cubic spinel structure with a space group (Fd-3 m) is established.

The lattice parameters *(a)* are calculated and found to be equal to 8.382 Å and 8.366 Å for $CoFe_2O_4$ and

Fig. 1 XRD diffraction pattern for CoFe$_2$O$_4$, Co$_{1.5}$Fe$_{1.5}$O$_4$, and ICDD card
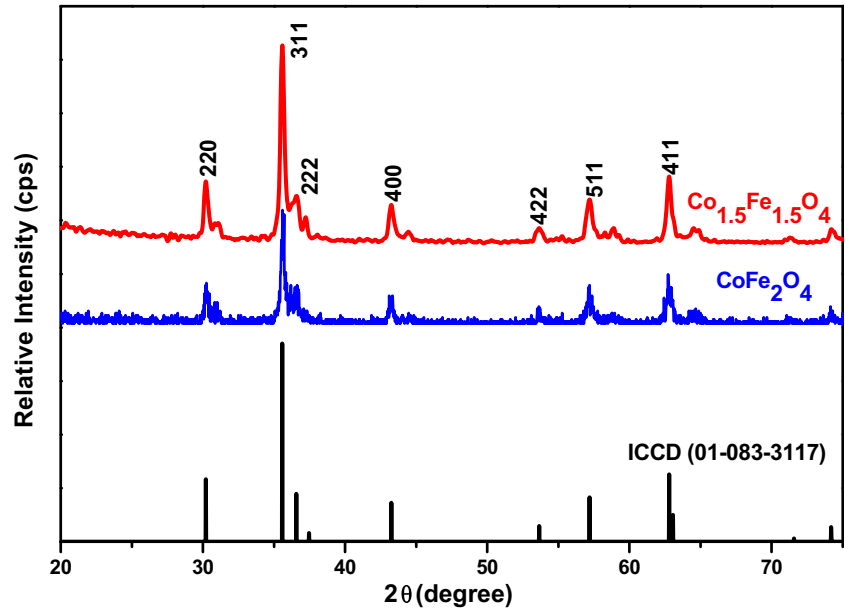
Co$_{1.5}$Fe$_{1.5}$O$_4$, respectively. The decrease in (a) as the ratio Co/Fe (> 0.5) increases is consistent with Vegard's law [15, 16].

In general, the increase and decrease in lattice parameter is dependent not only on the radius of cation content in the sample but also on other factors such as *i)* the percentage of oxygen vacancies and pores present in the composition; *(ii)* the type of the metal ions in A site compared with that in B site; and *(iii)* some ions prefer B site than A site, while others prefer A site over B site; additionally, some ions prefer to accommodate themselves in different ratios and radii in sites A and B.

In the present case, the composite contains different cations such as Fe^{3+} with ionic radii of 0.49, 0.645 °A in A and B sites, respectively. The Co^{2+} has ionic radii of 0.58A in the A site and 0.745A in the B site, and the Co^{3+} has ionic radii of 0.545 and 0.61 °A in the B site [15].

The correlation between the ionic radii and the theoretical lattice parameter (a_{th}) is determined using the following relation [17] and the calculated results are tabulated in Table 1

$$a_{th} = \frac{8}{3\sqrt{3}}\left[(r_A + R_O) + \sqrt{3}(r_B + R_O)\right], \qquad (1)$$

where r_A, r_B are the ionic radii of the A & B sites, respectively, and R$_o$ is the ionic radius of the oxygen ion (0.138 Å). The small deviation that appears between the a_{th} and the experimental $a_{exp.}$ is due to cation redistribution.

Table 1 Experimental lattice parameter (a), tolerance factor (T), Crystallite size (L), and X-ray density (Dx)

Samples	a_{exp} (Å)	a_{the} (Å)	T	L (nm)	D$_x$ (gm/cm^3)
CoFe$_2$O$_4$	8.382	8.385	0.99	37.73	5.295
Co$_{1.5}$Fe$_{1.5}$O$_4$	8.366	8.435	1.01	23.00	5.367

The average crystallite size of the sample (L) is calculated using the basic Debye–Scherer's equation [18] as mentioned in the previous work [19, 20], and the results are tabulated in Table 1. The broadening of the maximum intense peak corresponding to the (311) plane indicates that the investigated *NPs* crystallize in a nanosized scale. For CoFe$_2$O$_4$ and Co$_{1.5}$Fe$_{1.5}$O$_4$, the ratio of the cations in the *A/B* sites are ½ and 1.5/1.5 , respectively. It is clear that L drops from 37.73 nm to 23.00 nm as the ratio (Co^{2+}/Fe^{3+}) increases from 0.5 to 1. This is more likely related to the excess of nucleation centers. In other words, more crystals with smaller sizes are produced due to increasing nucleation rates on account of growth rates [21].

Additionally, this ratio in the case of Co$_{1.5}$Fe$_{1.5}$O$_4$ is greater than the theoretical/nominal one per formula. As a result, the occupancy of Fe in the B site is less than the theoretical value predicted by the formula. This finding ratifies the presence of the structural disorder in the spinel sublattices.

The oxygen positional parameter or anion parameter (u), which is the distance between the oxygen ion and the face of the cube edge along the cube diagonal of the spinel lattice, is calculated from the following equation [22].

$$u = \left[(r_A + R_o) / \left(a_{exp} \sqrt{3} \right) \right] + \frac{1}{4} \qquad (2)$$

It depends mainly on many factors such as the preparation environment, chemical composition, and the heating procedure used [21]. The average calculated values of "u" are 0.377 Å and ~ 0.381 Å for $CoFe_2O_4$ and $Co_{1.5}Co_{1.5}O_4$, respectively. The obtained 'u" parameter for a non-stoichiometric sample is greater than the standard one. This demonstrates that the $Co_{1.5}Fe_{1.5}O_4$ sample shows a comparatively small deviation from the authentic spinel ferrite.

The increase in u parameter could be due to the origin shifting at the A sites with an increase in the number of Fe (> 1) ions. This causes a small deviation from the FCC ideal case [7].

The Goldschmidt tolerance factor (T) for the synthesized powders is calculated using the following equation [23].

$$T = \frac{1}{\sqrt{3}} \left(\frac{r_A + R_O}{r_B + R_O} \right) + \frac{1}{\sqrt{2}} \left(\frac{R_O}{r_B + R_O} \right), \qquad (3)$$

where r_A and r_B are the ionic radii of the A and B sites, respectively, and R_O is the oxygen anion's ionic radius. The tolerance factor is found to be ≈ 1, which indicates that the prepared sample has a cubic spinel ferrite structure.

The theoretical density (D_x) is calculated as mentioned in the previous work [12, 24], and the calculated data are presented in Table 1. The increase in the value of the D_x for the prepared sample compared to that of $CoFe_2O_4$ is due to the difference in the atomic weight between Co^{2+} (58.933) and Fe^{3+} (55.845).

3.1.2 Scanning Electron Microscopy Analysis (SEM)

Scanning electron microscope (SEM) images of $CoFe_2O_4$ and $Co_{1.5}Fe_{1.5}O_4$ NPs are shown in Fig. 2 a-b. The grain shape of the investigated sample is roughly regular in shape and highly agglomerated. The average grain size is nearly equal to 32.5, 34.92 nm for $CoFe_2O_4$ and $Co_{1.5}Fe_{1.5}O_4$, respectively. There are several parameters affecting the grain size of the prepared samples such as variation of the pH

of the reaction [25], the total Fe/Co mole ratio [26], the rate of the reaction, and the sintering conditions [27]. The data agree well with the obtained data from XRD.

3.1.3 High-resolution transmission electron microscopy analysis (HRTEM)

HRTEM images and their selected area electron diffraction (SAED) ratify the construction of $CoFe_2O_4$ and $Co_{1.5}Fe_{1.5}O_4$ NPs with an average particle size of 39.37 nm as shown in Fig. 3. The NPs of $CoFe_2O_4$ have an almost regular size and spherical shape with limited hexagonal shape particles. Additionally, these NPs tended to agglomerate due to their magnetic nature. It is observed that the morphologies of cobalt with a stoichiometric ratio are more or less similar.

The image of $Co_{1.5}Fe_{1.5}O_4$ displays a hexagonal structure due to the distortion taking place from the cubic structure into a rhombohedral one. The tolerance factor is found to be 1.01. Thus, a small distortion occurs, leading to a lower symmetry structure. The SAED pattern reveals concentric rings that ratify the polycrystalline nature of the studied samples.

### 3.1.4 Energy-dispersive X-ray spectroscopy analysis (EDAX)

Figure 4 a–b demonstrates EDXA for the prepared samples. It confirms the presence of Fe, Co, and O ions in the examined sample. The low intensity peak at ≈ 0.25 keV is associated with the carbon (CKα) impurity characteristic line. This impurity is likely to have been introduced from the carbon-coated shields onto the pole pieces. The consistency between the obtained EDXA results and the expected chemical composition is appropriate as indicated in the internal table of the tested sample. The composition of the single phases Co/Fe = 0.5 and Co/Fe = 1 obtained with EDXA analysis agrees well with their starting elements. The surface crystal defects of the nanoparticle may be responsible for the discrepancy between the atomic ratio values reported by EDXA and the expected value.

3.1.5 Raman spectroscopy analysis (RSA)

RSA analysis can be used to determine the microstructure of materials down to the nanosized
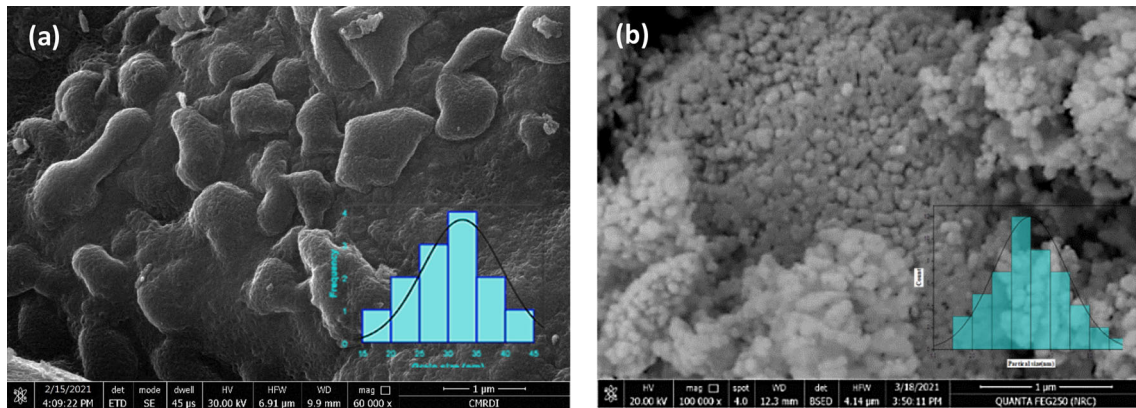
Fig. 2 a, b: SEM images for **a** CoFe$_2$O$_4$ **b** Co$_{1.5}$Fe$_{1.5}$O$_4$ ferrite nanoparticles. Insets: the histogram represents the size distribution for both samples
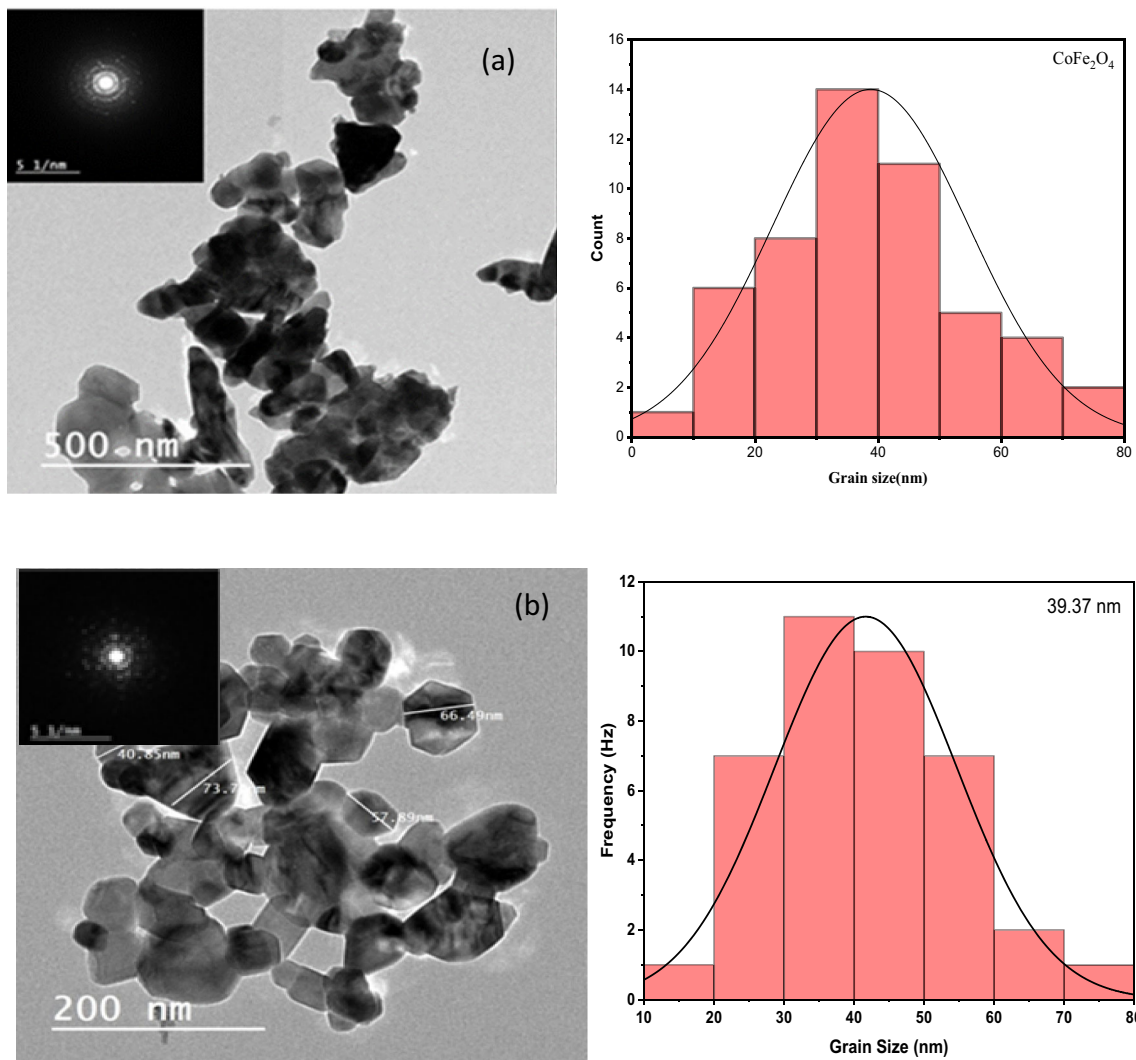
Fig. 3 a, b HRTEM with the SAED patterns for the **a** CoFe$_2$O$_4$ **b** Co$_{1.5}$Fe$_{1.5}$O$_4$ and histogram represents the size distribution
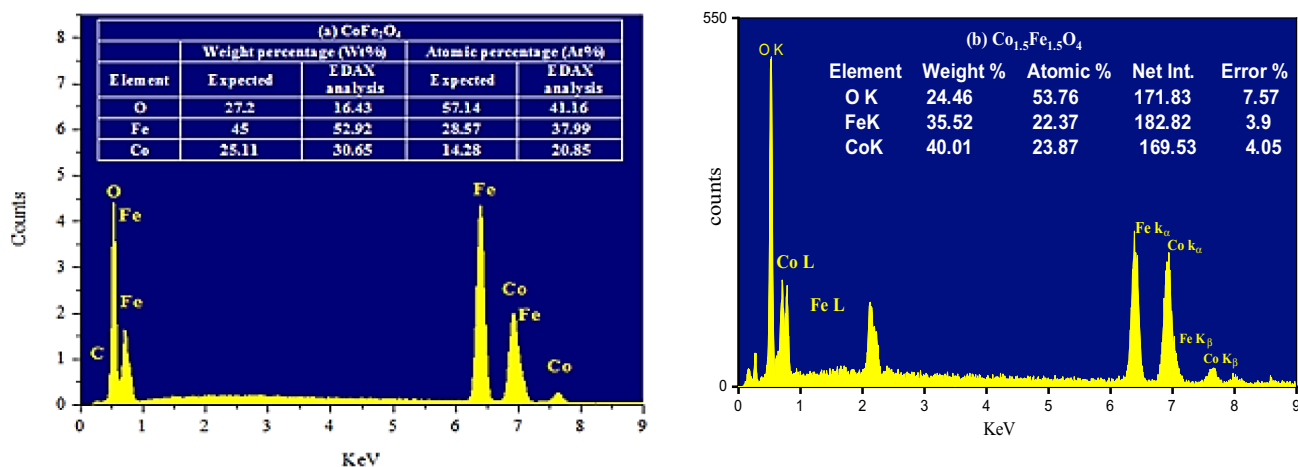
Fig. 4 a, b The EDXA spectrum for **a** CoFe$_2$O$_4$ and **b** Co$_{1.5}$Fe$_{1.5}$O$_4$

region. According to factor group analysis, there are 42 phonon modes (39 optical modes and 3 acoustic modes) [28]. The modes are A_{1g} (R), T_{1g}, E_g (R), $3T_{2g}$, (R2E$_u$,), $2A_{2u}$, $2T_{2u}$, and $4T_{1u}$ (IR) where (R) designates Raman active and (IR) designate infrared active vibrational species, while the remainder are quiet modes. As a result, only five modes A$_{1g}$, E$_g$, and 3T$_{2g}$ should be found in the RS of spinel ferrites, as shown in Fig. 5 [29].

The five Raman active modes (A_{1g}, $1E_g$, $3T_{2g}$) of CoFe$_2$O$_4$ and Co$_{1.5}$Fe$_{1.5}$O$_4$ are observed in the figure. The maxima appear and the assignment of these phonon modes are carried out in accordance with the literature reports [30]. In the testified structure samples, the modes above 600 cm^{-1} usually correspond to symmetric stretching of an oxygen atom with respect to the metal ion in the A site AO$_4$ group.

Thus, the three peaks at 606.1, 640, 665.4 cm^{-1} and 611.1, 636.7, 691.1 cm^{-1} signify A_{1g} symmetry for CoFe$_2$O$_4$ and Co$_{1.5}$Fe$_{1.5}$O$_4$, respectively. The other low-frequency phonon modes are due to metal ions involved in the octahedral void (BO$_6$), i.e., E$_g$ and 3T$_{2g}$. These modes correspond to the symmetric and antisymmetric bending of oxygen atoms at the octahedral void in the (metal–oxygen) M–O bond [31]. For CoFe$_2$O$_4$ and Co$_{1.5}$Fe$_{1.5}$O$_4$, three modes were obtained at approximately 189.1, 474.5, 540.3 cm^{-1}, and 226, 471.9, 572.7 cm^{-1}, respectively, which belong to the symmetry type T$_{2g}$. Also, it can be observed that the modes 245.4, 295.0 cm^{-1}, and 294.6 cm^{-1} for CoFe$_2$O$_4$ and Co$_{1.5}$Fe$_{1.5}$O$_4$ belong to the same symmetry, E$_g$. In general, the presence of vacancies, interstitial cations, and defects may result in the activation of new phonon modes in the non-
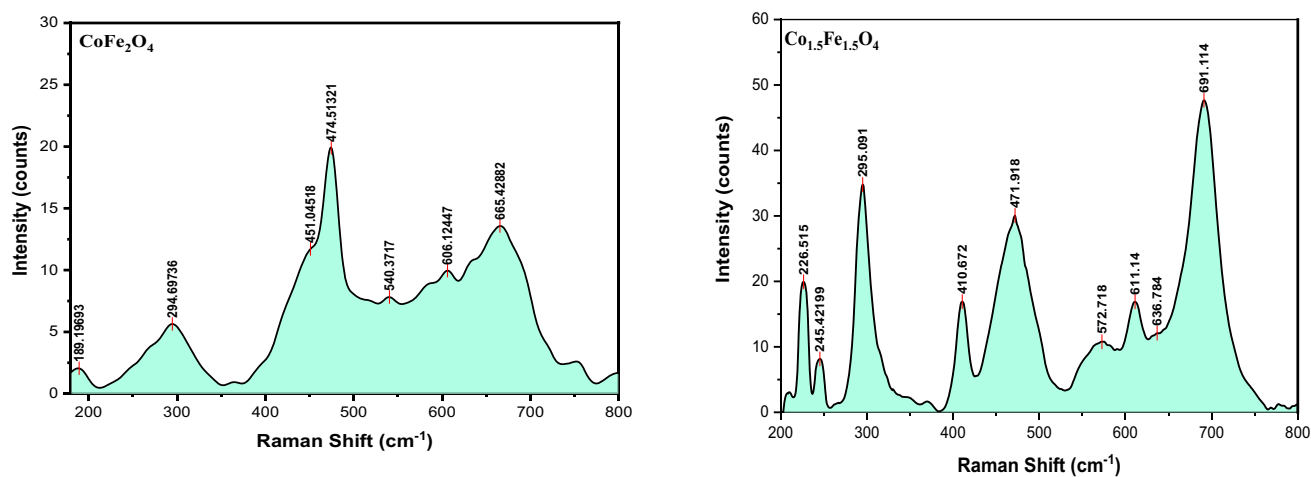
Fig. 5 a, b The Raman spectrum of CoFe$_2$O$_4$ and Co$_{1.5}$Fe$_{1.5}$O$_4$ samples

stoichiometric $Co_{1.5}Fe_{1.5}O_4$ not detected in stoichiometric $CoFe_2O_4$ samples. The cation distribution and its effect on the Raman spectrum of spinel have been extensively reviewed by Lazzeri et al. [32] and Wijs et al. [33]. Both studies have demonstrated the usefulness of Raman data in interpreting the cation redistribution in the spinel system.

3.1.6 X-ray photoelectron spectroscopy (Xps)

After analyzing the synthesized ferrite with EDAX data, the chemical composition of the ferrite is verified, and Co, Fe, and other elements are detected. For further study, XPS was performed to determine the oxidation state of each element and the chemical stoichiometry of the samples. The system properties change based on the oxidation state of the unpaired electrons.

The XPS wide scan spectra of $CoFe_2O_4$ and $Co_{1.5}Fe_{1.5}O_4$ nanoparticles are shown in Fig. 6. The binding energy values are used to find out the elements present in the sample. As shown in Fig. 6, the crystals contain Fe, Co, and O elements, and no other impurity elements are detected in the spectrum up to 1000 eV.

The high-resolution narrow scan XPS spectra of Fe 2p, Co 2p, and O 1 s peaks of the $CoFe_2O_4$ and $Co_{1.5}Fe_{1.5}O_4$ specimens are shown in Fig. 7 a–f, respectively. It can be observed that the 2p state energy level of the element is split into two energy levels, $2p_{3/2}$ and $2p_{1/2}$ energy levels, respectively, which is due to the spin orbit interactions. XPS can

also be used to detect two lattice positions in the spinel ferrite lattice [34].

Figure 7 a, d shows the Fe 2p core electron spectrum of the samples. The spectrum yields two asymmetric photoelectron peaks in the Fe 2p region, namely, Fe $2p_{1/2}$ peaks at 723.02 eV and 725.86 eV and the Fe $2p_{3/2}$ peaks at 710.49 eV and 713.88 eV, which reveal the presence of two non-equivalent bonds of Fe ions in the investigated sample. This indicates the presence of two kinds of lattice sites for the Fe ion occupancy in the investigated compound [35]. There are two faint satellite peaks at 718.25 eV and 732.22 eV, which are caused by the electronic transition caused by the charge transfer of Fe ions during the formation of ferrite [36]. According to these characteristics, the existence of Fe^{3+} ions in the investigated sample is confirmed. The presence of Fe^{2+} can be ruled out since no peaks are observed at about 708 eV and 709 eV [37, 38].

The doublets of Fe $2p_{3/2}$ at 710.49 eV and Fe $2p_{1/2}$ at 723.02 eV are due to the contributions from Fe^{3+} ions in the B sites, while the doublets of Fe $2p_{3/2}$ at 713.26 eV and Fe $2p_{1/2}$ at 725.86 eV are due to the contributions from Fe^{3+} ions in the A site [39].

The XPS spectra of Co $2p_{3/2}$ of the prepared samples are shown in Fig. 7 b, e. Inspection of the measured Co $2p_{3/2}$ shows two main doublets with peak positions at 779.59 eV and 781.75 eV. These are ascribed to Co^{2+} ions in the B site, and Co^{2+} ions in the A site, respectively. Another peak position at 785.52 eV is observed, indicating the presence of Co^{3+} ions in the B site. The B site is occupied by the majority of high spin Co^{2+} cations [40, 41]. The low
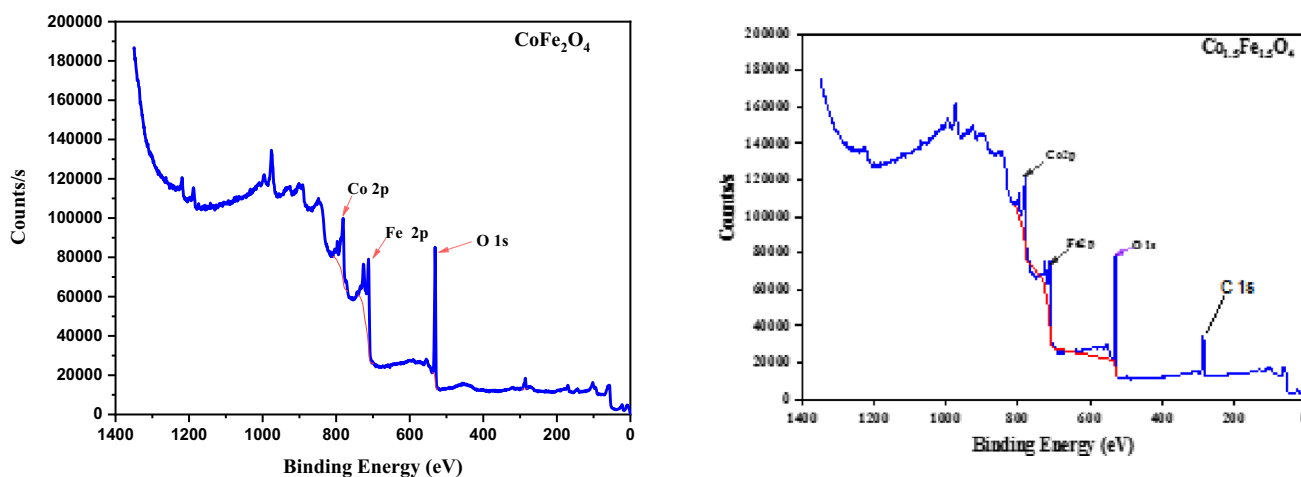
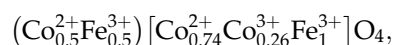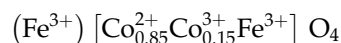**Fig. 6** The XPS spectrum of $CoFe_2O_4$ and $Co_{1.5}Fe_{1.5}O_4$ samples
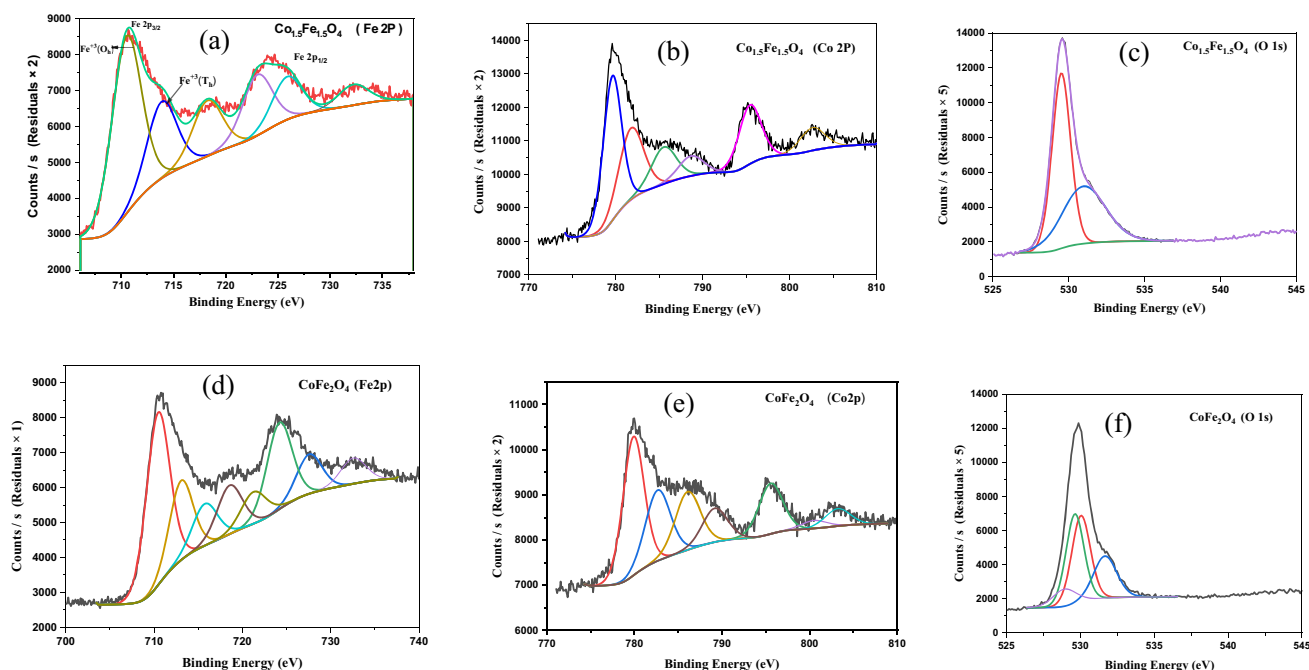
Fig. 7 a–f The XPS spectrum for Fe 2p, Co 2p, and O 1 s for both $CoFe_2O_4$ and $Co_{1.5}Fe_{1.5}O_4$ nanoparticles

spin Co^{3+} cation gives rise to a weaker satellite peak owing to the presence of unpaired valence electrons in the Co^{3+} orbital [40].

Figure 7 c, f shows the core level spectrum of O 1 s in the investigated samples. The main beak of the samples has 529.51 eV binding energy [33]. A second higher binding energy peak is found at 530.99 eV. From the above results, it is found that the sample can be represented by

$(Fe^{3+}) [Co^{2+}_{0.85} Co^{3+}_{0.15} Fe^{3+}] O_4$

$(Co^{2+}_{0.5} Fe^{3+}_{0.5}) [Co^{2+}_{0.74} Co^{3+}_{0.26} Fe^{3+}_1] O_4,$

where cations in parentheses () locate in the A site and those within square bracket [] in the B sites.

3.1.7 Atomic force microscopy (Afm)

AFM is utilized to examine the material's surface topography. The 2D and 3D AFM images of the $CoFe_2O_4$ and $Co_{1.5}Fe_{1.5}O_4$ NPs are shown in Fig. 8 a, b. The images reveal that the surface texture of both samples is wavy. In comparison to the valley, the hilly terrain is more rugged. The roughness of the sample under investigation can be quantitatively estimated by the root mean square roughness (R_{rms}) which is given by the standard deviation of the data

from the AFM image, and determined using the standard deviation as follows [42]:

$$R_{rms} = \sqrt{\frac{\sum_{n-1}^{N}(z_n - \overline{z})^2}{N-1}},\qquad(4)$$

where Z_n represents the height of the nth data, $\overline{Z}$ is the mean height of Z_n in AFM topography, and N is the number of data. The root mean square roughness is found to be 12.3 nm, while the roughness average is 8.59 nm.

3.2 Magnetic measurements

The magnetic character of cobalt NPs is better understood via VSM measurements, as shown in Fig. 9. The magnetic behavior of ferrimagnetic and ferromagnetic materials is very similar. In the strict definition of ferromagnetism, a material is ferromagnetic only if all of its magnetic ions are aligned and add a positive contribution to the net magnetization. However, if the number of spins is unequal (as in the present case), then the materials will be ferrimagnetic. Ferrimagnetism is observed only in compounds with complex crystal structures, such as ferrites. In the present samples, the spins on the Fe^{3+} sites cancel, because half of them are up and half are down. However, the three unpaired electrons of the
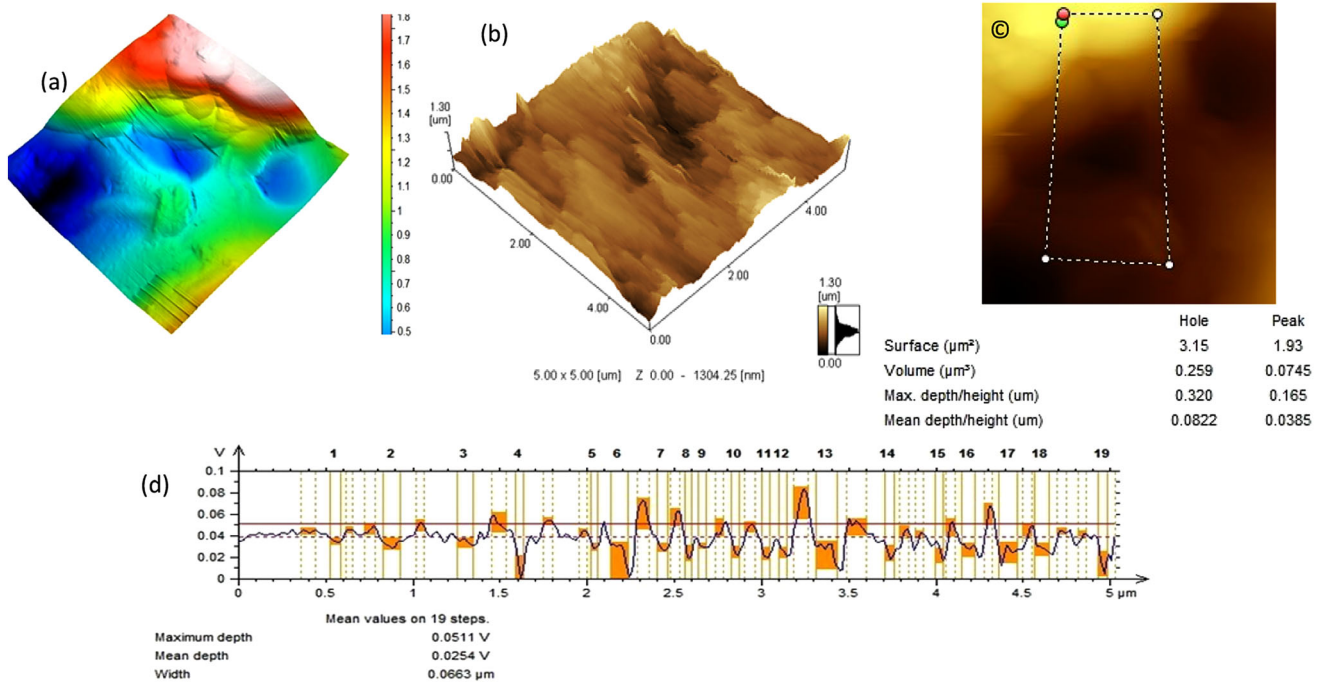
Fig. 8 The 2D and 3D AFM images for **a** $Co_{1.5}Fe_{1.5}O_4$ **b** $CoFe_2O_4$ NPs **c, d** More information about surface, volume, depth, and width for $Co_{1.5}Fe_{1.5}O_4$

Co^{2+} ions are all aligned the same way in the crystal, so the compound is ferrimagnetic [43].

The magnetic loop plots approve the ferrimagnetic behavior of $CoFe_2O_4$, and $Co_{1.5}Fe_{1.5}O_4$ NPs that are saturated with large values of magnetization depending on the stoichiometric/non-stoichiometric ratio for the (A cations /B cations).

The saturation magnetization M_s of $CoFe_2O_4$ and $Co_{1.5}Fe_{1.5}O_4$ NPs can be detected by an approximation of the Stoner–Wohlfarth theory by extrapolating the plot of M (emu/g) versus $1/H^2$ to approach zero [44, 45]. In this manner, the M_s value is equal to 66.8 & 48.15 emu/g for $CoFe_2O_4$ and $Co_{1.5}Fe_{1.5}O_4$, respectively. The obtained values and the experimental ones are very comparable to each other. This demonstrates that ± 20 kOe is a more suitable field to saturate the examined samples.

From the magnetic loops, the coercivity (H_C), saturation magnetization (M_S), remnant magnetization (Mr), squareness (Mr/Ms), and experimental magnetic moment (n_B) are calculated and summarized in Table 2.

Generally, the occupancy in A as well as B sites, spin/charge states, and content of transition metals play a significant role in the magnetic properties of the testified samples.

In ferrimagnetic materials that follow Neel's two-sublattice model, there can be three types of exchange interactions among the cations distributed in A sites and B sites sublattices, signified by A–A, A–B, and B–B interactions [46]. The A–B interaction is the highest one. The net magnetic moment for a spinel compound is taken as

$$M = M_B - M_A. \tag{5}$$

As shown from the table, $CoFe_2O_4$ exhibits maximum magnetic parameters. This behavior can be attributed to the cation concentration at the B site, which influenced the exchange interactions between A and B site cations and positively led to a higher maximum magnetization. On the other hand, for the $Co_{1.5}Fe_{1.5}O_4$ sample, the increase of Co (> 1) with lower magnetic moment on the expanse of Fe (< 2) with large magnetic moment decreases the magnetic parameters of the system.

For the testified sample, M depends on the number of unpaired spins of the Co & Fe ions, their charge, the spin states of the transition metal ions as well as the distribution of cobalt, and iron ions between A and B sites, as mentioned in the previous work [47]. The number of unpaired spins for all used ions in
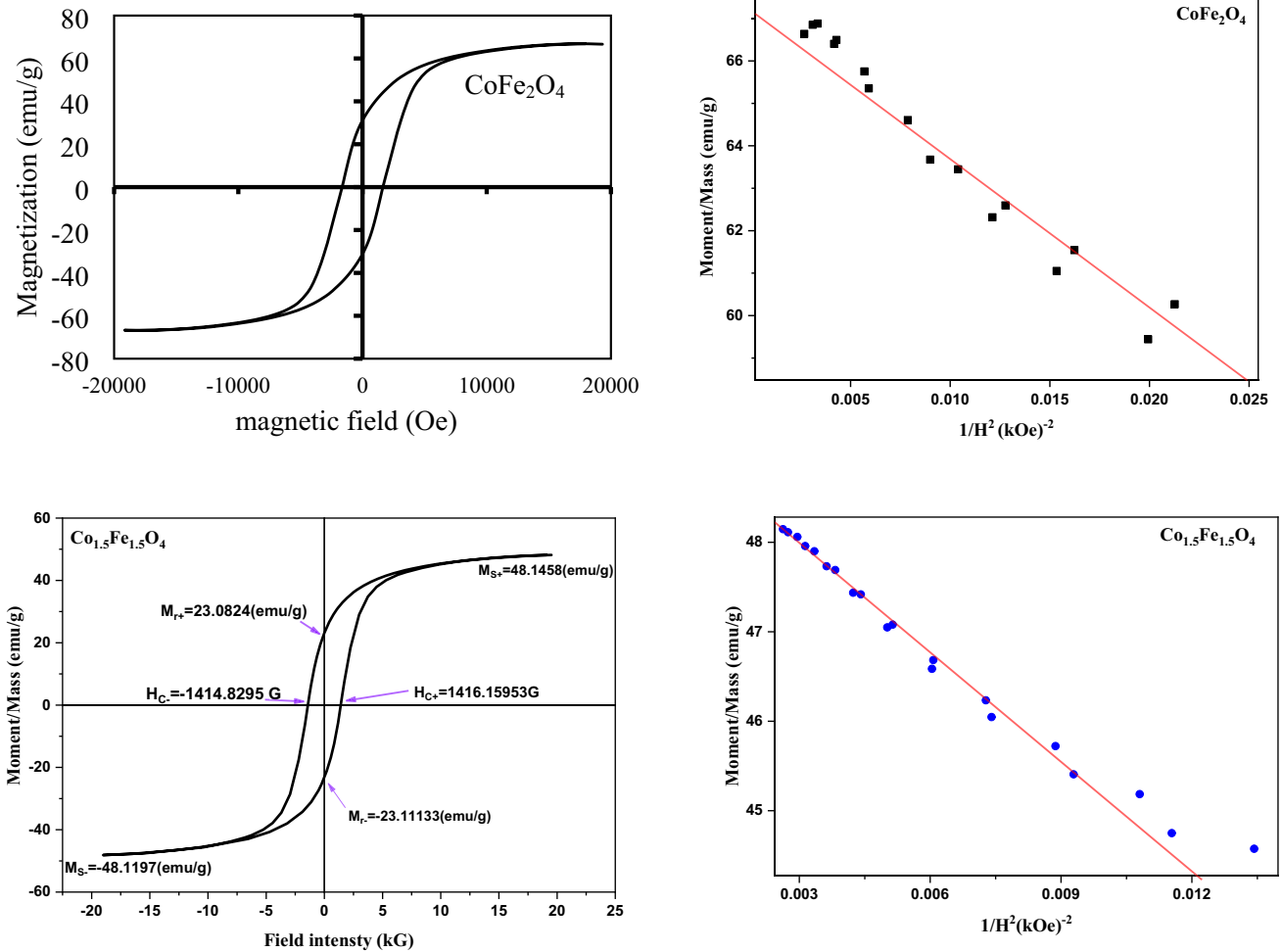
Fig. 9 The magnetic Hysteresis loops for $CoFe_2O_4$ and $Co_{1.5}Fe_{1.5}O_4$, and fitting plot between M versus $1/H^2$

Table 2 Values of the magnetic parameters obtained from hysteresis loop

Samples	M_s (emu/g)	M_r (emu/g)	H_c (Oe)	M_r/M_s	Energy loss (erg./g)	size	n_B exp
$CoFe_2O_4$	66.847	31.114	1641	0.465	337.11	37.73	2.808
$Co_{1.5}Fe_{1.5}O_4$	48.142	23.094	1415	0.479	204.69	23	2.035

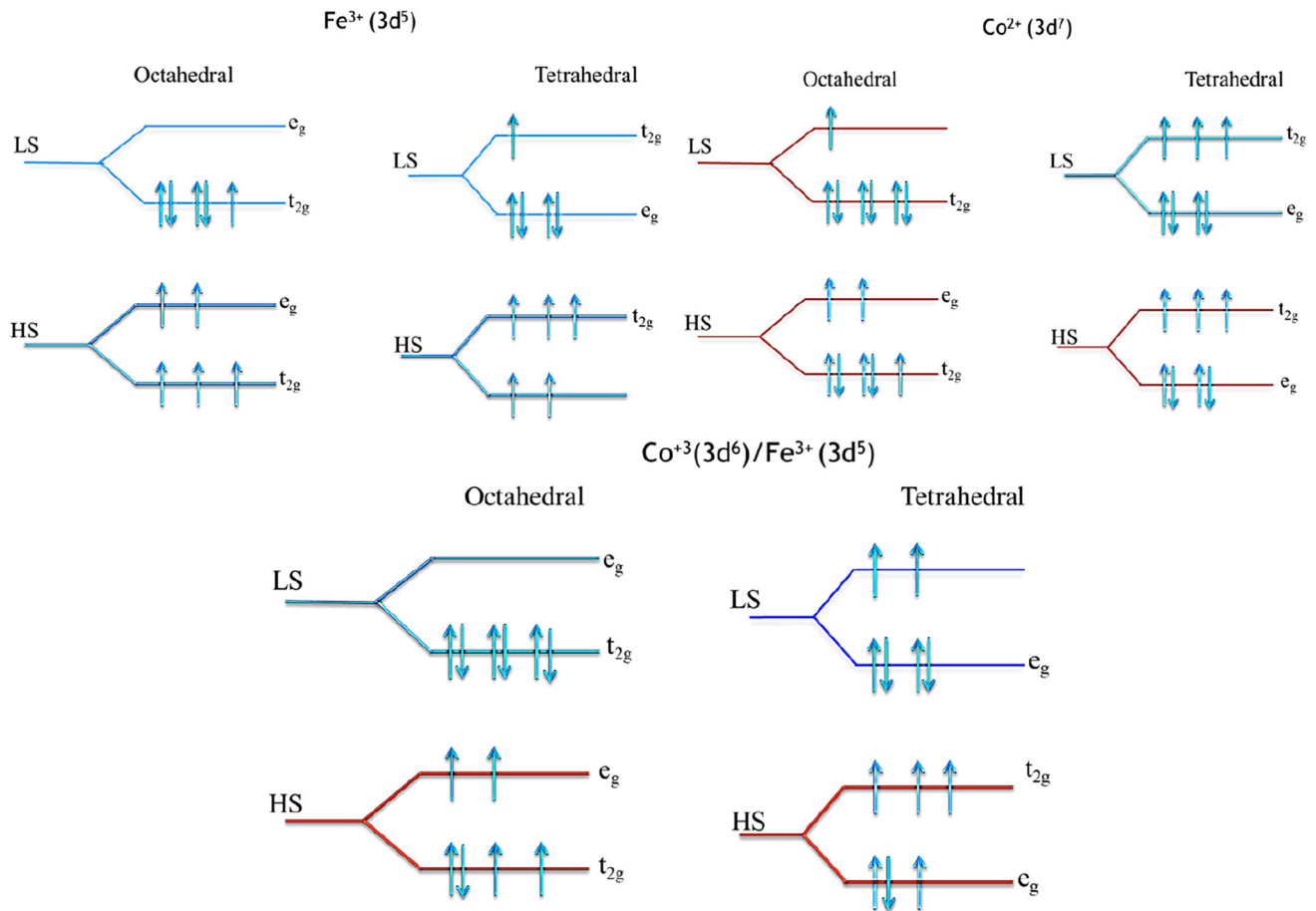high spin as well as low spin configurations is detected in Fig. 10 [48, 49].

However, the spin states of Co^{2+} ($3d^7$), Co^{3+} ($3d^6$) ions in the B site have been proposed to be in both high spin [50, 51] and low spin states, respectively [52].

Co^{2+} ($3d^7$) in the A site is typically found in a high spin state [53, 54]. On other hand, Fe^{3+} ($3d^5$) in the B site and Fe^{3+} ($3d^5$) in A sites are frequently found in high spin states [55]. According to the previous discussion, the calculated magnetic moment for the $CoFe_2O_4$ spinel ferrite equals 2.808 which is higher than the 2.035 emu/g calculated for $Co_{1.5}Fe_{1.5}O_4$.

The magnetic moment per molecule in the Bohr magneton (Table 3.2) for each sample is calculated using the following equation:

$$n_B = \frac{M \times M_s}{5585}, \qquad (6)$$

where M is the molecular weight of the sample. The obtained values are less than the theoretical value. The small differences in the values are due to the slight change in cation distribution of both [A] and [B] sites [56]. Moreover, it may relate to the surface spins canting, in which spins are tilted by a narrow angle about their axis.

Fig. 10 The low spin and high spin configuration for tetrahedral and octahedral sites

The reduction in the magnetization with an increase in the Co/Fe ratio = 1 is anticipated. Since the "extra" Co will incorporate at the B sublattice, leading to a decline in its magnetic moment. The magnetization of the system may be further decreased due to a large number of point defects existing in the spinel structure due to the non-stoichiometry. In the $Co_{1.5}Fe_{1.5}O_4$, oxygen vacancies should be present. These vacancies disrupt the super-exchange interaction between magnetic ions, consequently decreasing the magnetization of the sample's NPs.

In contrast, iron and cobalt are distributed between the A and B sites according to the stoichiometric ratio (1Fe / 2Fe Co = 0.5). The magnetic moment of the A site will decrease. Consequently, the difference between the two sites (A–B) will increase, which leads to an increase in magnetization of the system.

Furthermore, the SQR (M_r/M_s) values are found in the range of 0.465–0.479 which can be ascribed to surface spin disorder effects as well as to the

formation of a multi-magnetic domain. The results verify that the particle size can control H_C. Moreover, H_C is very sensitive to the NPs size, distribution characteristics, morphology, surface spin, and inter-particle interaction.

4 Conclusion

XRD for the investigated samples confirmed the formation of a single-phase cubic spinel structure with a space group (Fd-3 m).

HRTEM images and their selected area electron diffraction (SAED) ratified the construction of $CoFe_2O_4$ and $Co_{1.5}Fe_{1.5}O_4$ NPs with an average particle size of 39.37 nm. XPS results provided the cation chemical states of Fe^{2+}, Fe^{3+} and Co^{2+}, Co^{3+}, as well as their occupation ratio between A and B sites. The magnetic change is related to the radius of the ion, the size of the particle, and the exchange effect existing in the crystal lattice.

The calculated magnetic moment for the $CoFe_2O_4$ spinel ferrite equals 2.808, which is greater compared to the calculated magnetic moment of $Co_{1.5}Fe_{1.5}O_4$.

The SQR (M_r/M_s) values are found in the range of 0.465–0.479, which can be ascribed to surface spin disorder effects as well as to the formation of a multi-magnetic domain.

5 Future work

The numerous uses of $Mg_{0.85}$ $K_{0.3}Fe_2O_4$/GO spinel nanoferrite particles will be the main issue for future work. The main advantages of the synthesized sample are ease of separation, high adsorption, low cost, and recyclable with notable efficiency. Thus, it is suggested as a promising candidate for wastewater treatment [57, 58].

The cheap and non-toxic $Mg_{0.85}$ $K_{0.3}Fe_2O_4$/GO spinel nanoferrite particles can be employed as an anode for lithium-ion batteries (LIBs). It is able to demonstrate superior electrochemical performance in terms of specific capacity, cycle performance, and rate capability [59].

In addition, potassium ferrite is a good candidate for biomedical application, as iron and potassium are biocompatible and non-toxic materials [60].

Acknowledgements

Author contributions

EEA: Investigation, Formal analysis, Data curation, Writing—original draft, Data analysis, review & editing. BH: Conceptualization, Investigation, Validation, Visualization, Data curation, and Writing—review & editing. AAL-H: Methodology, Optimum selection of material parameters, Formal analysis, XRD analysis, and Writing—review & editing.

Funding

Data availability

The datasets generated during and/or analyzed during the current study are available from the corresponding author on reasonable request.

Code availability

Not applicable.

Declarations

Conflict of interest The authors declare that they have no conflict of interest.

Ethical approval Not applicable.

Consent to participate The corresponding author signs and accepts the responsibility for releasing this research on behalf of any and all co-authors. Besides, all the authors approved the final version of the manuscript.

Consent for publication I understand that the data collected from my participation will be used for journal publication and I consent for it to be used in that manner.

References

1. E.E. Ateia, M.A. Ateia, M.M. Arman, Assessing of channel structure and magnetic properties on heavy metal ions removal from water. J. Mater. Sci. Mater. Electron. **33**, 8958 (2022)
2. J. Hu, X. Liu, X. Kan, S. Feng, C. Liu, W. Wang, K.M.U. Rehman, M. Shazed, S. Zhou, Q. Wu, Characterization of texture and magnetic properties of $Ni_{0.5}Zn_{0.5}Ti_xFe_{2-x}O_4$ spinel ferrites. J. Magn. and Magn. Mater. **489**, 165411 (2019)
3. B.R. Babu, T. Tatarchuk, Elastic properties and anti-structural modeling for Nickel-Zinc Ferrite-Aluminates. Mater. Chem. Phys. **207**, 534 (2018)
4. K.K. Kefeni, B.B. Mamba, T.A.M. Msagati, Application of spinel ferrite nanoparticles in water and wastewater treatment: a review. Sepal. Purif. Technol. **188**, 399 (2017)
5. S. Bashir, ed. Advanced Electromagnetic Waves, (2015) ISBN-13: 978–9535122050.

6. S. Gul, M.A. Yousuf, A. Anwar, M.F. Warsi, P.O. Agboola, I. Shakir, M. Shahid, Al-substituted zinc spinel ferrite nanoparticles: preparation and evaluation of structural, electrical, magnetic and photocatalytic properties. Ceram. Int. **46**, 14195 (2020)

7. O.M. Hemeda, Structural and magnetic properties of $Co_{0.6}Zn_{0.4}Mn_xFe_{2-x}O_4$. Turk. J. Phys. **28**, 121 (2004)

8. M. Margabandhu, S. Sendhilnathan, S. Senthilkumar, D. Gajalakshmi, Investigation of structural, morphological, magnetic properties and biomedical applications of Cu^{2+} substituted uncoated cobalt ferrite nanoparticles. Braz. Arch. Biol. Technol. **59**, e161046 (2016)

9. A.F. Junior, V. Zapf, P. Egan, Magnetic properties of nanoparticles of $Co_xFe_{3-x}O_4$ ($0.05 \leq x \leq 1.6$). J. Appl. Phys. **101**, 09M506 (2007)

10. Y.H. Hou, Y.J. Zhao, Z.W. Liu, H.Y. Yu, X.C. Zhong, W.Q. Qiu, D.C. Zeng, L.S. Wen, Structural, electronic and magnetic properties of partially inverse spinel $CoFe_2O_4$: a first-principles study. J. Phys. D: Appl. Phys. **43**, 445003 (2010)

11. U. Megha, K. Shijina, G. Varghese, Nanosized $LaCo_{0.6}Fe_{0.4}O_3$ perovskites synthesized by citrate sol gel auto combustion method. Process. Appl. of Ceram. **8**, 87 (2014)

12. E.E. Ateia, G. Abdelatif, F.S. Soliman, Optimizing the physical properties of calcium nanoferrites to be suitable in many applications. J. Mater. Sci. Mater. Electron. **28**, 5846 (2017)

13. E.E. Ateia, R. Ramadan, B. Hussein, Studies on multifunctional properties of $GdFe_{1-x}Co_xO_3$ multiferroics. Appl. Phys. A: Materials Sci. and Processing **126**, 340 (2020)

14. N.V. Praskurina, V.A. Cherepanov, O.S. Galynts, V.I. Voronin, Inorg. Mater. **40**, 955 (2004)

15. N. Ahmad, S. Khan, M.M.N. Ansari, Optical, dielectric and magnetic properties of Mn doped SnO_2 diluted magnetic semiconductors. Ceram. Int. **44**, 15972 (2018)

16. A.R. Denton, N.W. Ashcroft, Vegard's law. Phys. Rev. A **43**, 3161 (1991)

17. Z. Zhou, Y. Zhang, Z. Wang, W. Wei, W. Tang, J. Shi, R. Xiong, Electronic structure studies of the spinel $CoFe_2O_4$ by X-ray photoelectron spectroscopy. Appl. Surf. Sci. **254**, 6972 (2008)

18. P. Scherrer, Bestimmung der Grösse und der inneren Struktur von Kolloidteilchen mittels Röntgenstrahlen. Nachr. Ges. Wiss. Göttingen **26**, 98 (1918)

19. E.E. Ateia, A.T. Mohamed, Core–shell nanoarchitectonics of $CoFe_2O_4$ encapsulated $La_2Fe_2O_6$ Nanoparticles for their use in various applications. J. Inorg. Organomet. Polym. Mater. **32**, 1389 (2022)

20. E.E. Ateia, A.T. Mohamed, K. Elsayed, Impact of Gd^{3+}/-graphene substitution on the physical properties of magnesium ferrite nanocomposites. J. Magn. Magn. Mater. **452**, 169 (2018)

21. S.H. Lafta, The relation of crystallite size and Ni^{2+} content to ferromagnetic resonance properties of nano nickel ferrites. Journal of Magnetics **22**, 188 (2017)

22. O.M. Hemeda, A. Tawfik, A.M.A. Henaish, B.I. Salem, Strong correlations between structural and magnetic properties of Zn and Zr substituted $CuFe_2O_4$ for magnetic temperature controller applications. Arab J. Nucl. Sci. Appl. **51**, 22 (2018)

23. A.M. Wahba, M.B. Mohamed, Structural, magnetic, and dielectric properties of nanocrystalline Cr-substituted $Co_{0.8}Ni_{0.2}Fe_2O_4$ ferrite. Ceram. Int. **40**, 6127 (2014)

24. M.M. Arman, M.A. Ahmed, Effects of vacancy co-doping on the structure, magnetic and dielectric properties of $LaFeO_3$ perovskite nanoparticles. Appl. Phys. A Mater. Sci. Process. **128**, 554 (2022)

25. Ur.R. Atta, "Synthesis and Characterization of Cobalt Ferrite Nanostructures", (doctoral dissertation, Pakistan Institute of Engineering and Applied Science, Islamabad) (2014).

26. C.N. Chinnasamy, M. Senoue, B. Jeyadevan, O.P. Perez, K. Shinoda, K. Tahji, Synthesis of size-controlled cobalt ferrite particles with high coercivity and squareness ratio. J. Colloid Interface Sci. **263**, 80 (2003)

27. L. Wang, Q. Zhang, Effect of Fe^{3+}/Ba^{2+} mole ratio on the phase formation and microwave properties of $BaFe_{12}O_{19}$ prepared by citrate–EDTA complexing method. J. Alloy. Compd. **469**, 251 (2009)

28. V. D'Ippolito, G.B. Andreozzi, D. Bersani, P.P. Lottici, Raman fingerprint of chromate, aluminate and ferrite spinels. J. Raman Specrosc. **46**, 1255 (2015)

29. W.B. White, B.A. DeAngelis, Interpretation of the vibrational spectra of spinels. Spectrochim. Acta, Part A **23**, 985 (1967)

30. P.R. Graves, C. Johnston, J.J. Campaniello, Raman scattering in spinel structure ferrites. Mater. Res. Bull. **23**, 1651 (1988)

31. Z. Wang, P. Lazor, S.K. Saxena, H.S.C. O'Neill, High pressure Raman spectroscopy of ferrite $MgFe_2O_4$. Mater. Res. Bull. **37**, 1589 (2002)

32. M. Lazzeri, P. Thibaudeau, Ab initio Raman spectrum of the normal and disordered $MgAl_2O_4$ spinel. Phys. Rev. B **74**, 140301 (2006)

33. G.A. de Wijs, C.M. Fang, G. Kresse, G. de With, First-principles calculation of the phonon spectrum of $MgAl_2O_4$ spinel. Phys. Rev. B **65**, 094305 (2002)

34. R.S. Yadav, I. Kuřitka, J. Vilcakova, J. Havlica, J. Masilko, L. Kalina, J. Tkacz, V. Enev, M. Hajdúchová, Structural, magnetic dielectric and electrical properties of $NiFe_2O_4$ spinel ferrite nanoparticles prepared by honey-mediated sol–gel combustion. J. Phys. Chem. Solids **107**, 150 (2017)

35. P. Liu, H. He, G. Wei, X. Liang, F. Qi, F. Tan, W. Tan, J. Zhu, R. Zhu, Effect of Mn substitution on the promoted formaldehyde oxidation over spinel ferrite: catalyst characterization, performance and reaction mechanism. Appl. Catal. B: Environ **182**, 476 (2016)

36. M.V. Bukhtiyarova, A.S. Ivanova, E.M. Slavinskaya, L.M. Plyasova, V.A. Rogov, V.V. Kaichev, A.S. Noskov, Catalytic combustion of methane on substituted strontium ferrites. Fuel **90**, 1245 (2011)

37. M.C. Biesinger, B.P. Payne, A.P. Grosvenor, L.W. Lau, A.R. Gerson, R.S.C. Smart, Resolving surface chemical states in XPS analysis of first row transition metals, oxides and hydroxides: Cr, Mn, Fe, Co and Ni. Appl. Surf. Sci. **257**, 2717 (2011)

38. A.P. Grosvenor, B.A. Kobe, M.C. Biesinger, N.S. McIntyre, Investigation of multiplet splitting of Fe 2p XPS spectra and bonding in iron compounds. Surf. Interface Anal. **36**, 1564 (2004)

39. J. Song, Z. Wang, Y. Gao, Effect of heat treatment on structural and magnetic properties of Li–Ni ferrite prepared via sol–gel auto-combustion method. J. Mater. Sci. Mater Electron. **32**, 17105 (2021)

40. J.-G. Choi, L.T. Thompson, XPS study of as-prepared and reduced molybdenum oxides. Appl. Surf. Sci. **93**, 143 (1996)

41. J.-G. Kim, D.L. Pugmire, D. Battaglia, M.A. Langell, Analysis of the $NiCo_2O_4$ spinel surface with Auger and X-ray photoelectron spectroscopy. Appl. Surf. Sci. **165**, 70 (2000)

42. P. Vlazan, M. Vasile, Synthesis and characterization $CoFe_2O_4$ nanoparticles prepared by the hydrothermal method. Optoelectron. Adv. Mat-Rapid Commun. **4**, 1307 (2010)

43. C.K. Jorgensen, *Modern aspects of ligand field theory* (North Holland Publishing, Amsterdam, 1971)

44. A. Baykal, S. Esir, A. Demir, S. Güner, Magnetic and optical properties of $Cu_{1-x}Zn_xFe_2O_4$ nanoparticles dispersed in a silica matrix by a sol–gel auto-combustion method. Ceram. Int. **41**, 231 (2015)

45. S. Güner, Md. Amir, M. Geleri, M. Sertkol, A. Baykal, Magneto-optical properties of Mn^{3+} substituted Fe_3O_4 nanoparticles. Ceram. Int. **41**, 10915 (2015)

46. F. Nakagomi, S.W. da Silva, V.K. Garg, A.C. Oliveira, P.C. Morais, A.F. Junior, E.C.D. Lima, The ingluence of Cobalt population on the structural properties of $Co_xFe_{3-x}O_4$. J. Appl. Phys **101**, 09M514 (2007)

47. A. Kiswandhi, J.S. Brooks, J. Lu, J. Whalen, T. Siegrist, H.D. Zhou, Chemical pressure effect on structural, magnetic and transport properties of $Mn_{1-x}Co_xV_2O_4$. Phys. Rev. B **84**, 205138 (2011)

48. E.E. Ateia, E. Takla, A.T. Mohamed, Physical and magnetic properties of (Ba/Sr) substituted magnesium nano ferrites. Appl. Phys. A **123**, 631 (2017)

49. Y. Ding, D. Haskel, S.G. Ovchinnikov, Y.C. Tseng, Y.S. Orlov, J.C. Lang, H.K. Mao, Novel pressure-induced magnetic transition in Magnetite (Fe_3O_4). Phys. Rev. Lett. **100**, 045508 (2008)

50. E.W. Gorter, Saturation magnetization and crystal chemistry in ferromagnetic oxides. Philips Res. Rep. **9**, 295 (1954)

51. J.S. Griffiths, *The theory of transition metal ions* (Cambridge University Press, 1961)

52. O. Gunnarson, O.K. Andersen, O. Jespen, J. Zannen, Density-functional calculation of the parameters in the Anderson model: application to Mn in CdTe. Phys. Rev. B **39**, 1708 (1989)

53. S.G. Fritsch, C. Tenailleau, H. Bordeneuve, A. Rousset, Magnetic properties of cobalt and manganese oxide spinel ceramic. Adv. Sci. Techn. **67**, 143 (2010)

54. N.V. Thanh, N.T. Nguyet, N.A. Tuan, Geometric structure, electronic structure and spin transition of Fe^{2+} spin-crossover molecules. Proc. Natl. Conf. Theor. Phys. **36**, 256 (2011)

55. A. Bengston, D. Morgan, U. Becker, Spin states of iron in Fe_3O_4 magnetite and h-Fe_3O_4. Phys. Rev B **87**, 155141 (2013)

56. K. Ramakrishna, Ch. Srinivas, S. Meena, B. Tirupanyam, P. Bhatt, S. Yusuf, C. Prajapat, D.M. Potukuchi, D.L. Sastry, Investigation of cation distribution and magneto crystalline anisotropy of $Ni_xCu_{0.1}Zn_{0.9-x}Fe_2O_4$ nano ferrites. Ceram. Int. **43**, 7984 (2017)

57. E.E. Ateia, R. Ramadan, A.S. Shafaay, Efficient treatment of lead-containing wastewater by $CoFe_2O_4$/ graphene nanocomposites. Appl. Phys. A **126**, 222 (2022)

58. E.E. Ateia, K. Elsayed and R. Ramadan, (2022). "Tuning the Properties of Ba-M Hexaferrite $BaFe_{11.5}Co_{0.5}O_{19}$: A Road Towards Diverse Application", J. Inorg. Organomet. Polym. Mater.

59. E.E. Ateia, M.A. Ateia, M.G. Fayed, S.I. El-Hout, S.G. Mohamed, M.M. Arman, Synthesis of nanocubic lithium cobalt ferrite toward high-performance lithium-ion battery. Appl. Phys. A **128**, 483 (2022)

60. S.R. Mokhosi, W. Mdlalose, A. Nhlapo, M. Singh, Advances in the Synthesis and Application of Magnetic Ferrite Nanoparticles for Cancer Therapy. Pharmaceutics **14**, 1405093 (2022)